J. Ocean Univ. China (Oceanic and Coastal Sea Research)
https://doi.org/10.1007/s11802-019-3885-7
ISSN 1672-5182, 2019 18 (3): 596-604
http://www.ouc.edu.cn/xbywb/
E-mail:xbywb@ouc.edu.cn

A Correction Algorithm for Atmospheric Visibility Based on Fog Droplet Size Data Obtained on a Moving Ship During 2016 Arctic Cruise

LIU Yilin[1)], and ZHAO Jinping[1), 2), *]

1) *College of Oceanic and Atmospheric Sciences, Ocean University of China, Qingdao* 266100, *China*
2) *Key Laboratory of Physical Oceanography, Ocean University of China, Qingdao* 266100, *China*

(Received April 10, 2018; revised August 13, 2018; accepted September 18, 2018)

Abstract In this study, we measured the droplet size distribution (DSD) and visibility of sea fog using a fog droplet spectrometer and visibility meter, respectively, during the July 23–August 3 and August 22–September 13 periods of the 2016 Chinese National Arctic Research Expedition. We calculated the visibility using the Mie theory and the DSD data and then compared the calculated with the observed visibility. The comparison shows that the deviations in the calculated visibility caused by DSD data sampling errors cannot be ignored. During navigation, wind and ship speeds tended to push or pull the sampled air and cause turbulence pulsation, which influenced the sampling of the fog droplet spectrometer. This influence is weak when the liquid water content (LWC) is high but becomes stronger as the LWC decreases. Taking the sailing speed and heading into consideration, the wind speed component parallel and perpendicular to the air inlet of the fog droplet spectrometer exhibit different laws in the deviation. By performing a fitting analysis of the calculated and observed visibilities under different wind speeds and wind directions, here, we present two sets of correction coefficients for the two wind-speed components and a method for correcting the calculated visibility. This correction method shows excellent results.

Key words Arctic sea fog; fog droplet size distribution; liquid water content; visibility; Mie theory

1 Introduction

Sea fog refers to weather phenomena that are affected by the ocean and appear on the sea (including coasts and islands), with a resulting visibility of less than 1000 m (Wang, 1983). Sea fog is a type of disastrous ocean weather that occurs due to the condensation of water vapor into liquid water. This causes a sharp decline in visibility that seriously affects human activities such as fishing and transportation at sea and on adjacent land, and also interferes with communications and even military operations. In addition, the time period and area of sea fog are important reference factors for route selection. It can be said that sea fog closely affects every aspect of human activity. As such, research on the physical mechanism of sea fog has both theoretical significance and application value.

The most important influence of fog on human life is the attenuation of visibility. When fog occurs, visibility is rapidly reduced from tens of thousands of meters to hundreds or even tens of meters. Research on sea fog visibility is essentially the study of the scattering effect of sea fog droplets on natural light. To study the scattering effect, direct observation of these droplets is necessary. Houghton and Radford (1938) made a large number of observations on coastal and mountain fogs using a device that can capture and then photograph droplets on a glass slide, from which they determined the relationship between liquid water content (LWC) and visibility. Since that early study, fog droplet data has been increasingly applied to research on land and sea fogs, especially the relationship between the droplet size distribution (DSD) and visibility. The visibility calculated using the Mie theory and DSD data collected in the Arctic is very close to the observed visibility (Kumai, 1973). We know that droplets of different sizes contribute differently to the LWC and visibility attenuation. That is, small droplets contribute more to the decline of visibility than to LWC, whereas large droplets do the opposite (Garland, 1971; Roach, 1976). In recent years, great progress has been made in the study of sea fog. However, researchers have often focused on the sea areas around countries and have paid less attention to the Arctic. The impact of sea fog on the Arctic sea ice and upper oceans cannot be ignored, given that the Arctic is one of the regions with the highest occurrences of sea fog (Venne *et al.*, 1997). From the study of Arctic clouds, we can see that increased cloud cover will strengthen Arctic

* Corresponding author. Tel: 0086-532-66782096
E-mail: jpzhao@ouc.edu.cn

warming by reducing the net upward long-wave radiation of sea ice and the sea surface (Shupe and Intrieri, 2004; Palm *et al.*, 2010). Both cloud and fog droplets evolve from condensation nuclei in saturated vapor. Their similar formation processes mean that they have some similarities, and low clouds and fog can be transformed from one to the other with changes in height (Gultepe *et al.*, 2007). However, in some cloud research, to avoid the impact of the underlying surface, low-altitude weather processes are typically overlooked, thus ignoring the role of fog in the Arctic ocean and atmosphere (Gultepe *et al.*, 2014).

Most of the data used in sea fog studies have been collected from islands and coastal cities. These data were affected in different degrees by sea and land fogs under different wind speeds and directions. In fact, with respect to the observation method, most of our understanding of the microphysical structure of sea fog is based on our previous understanding of land fog. Generally, sea fog observation methods rely on land observation stations. Even when data is collected from coastal cities and islands, the impact of land cannot be ignored (Koračin *et al.*, 2014). Analyses of the residue after the evaporation of sea fog droplets has shown that combustion nuclei with radii of less than 1 μm play a major role in the sea fog condensation process. Sea-salt particles are not the major source of condensation nuclei (Ogiwara and Okita, 1952). Previous studies show that sea fog data collected on the coast are more or less affected by the land environment. Due to factors such as land dust and environmental pollution, the volume of combustion nuclei and dust in land fog is much greater than that in sea fog (Wang, 1983), which provides rich condensation nuclei for fogging. Therefore, sea fog data collected during navigation is worthy of study.

In this study, we used DSD data collected from 2016 Chinese National Arctic Research Expedition to calculate visibility by the Mie theory. We found the deviation between the calculated and observed visibilities to be large. We determined the relationships of the deviation, wind speed, wind direction, ship speed and ship heading and propose a method for correcting the calculated visibility of Arctic ship-based sea fog observations.

2 Measurement Instruments, Data, and Method

2.1 Measurement Instruments and Data

For the sea fog data obtained during the 2016 Chinese Arctic Scientific Expedition, we used two instruments. The DSD data were sampled by an FM-120 fog droplet spectrometer manufactured by Droplet Measurement Technologies, USA. The DSD is determined by active ventilation at sampling intervals ranging from 0.04 to 20 seconds, with 1 second chosen for this study. The droplet diameter ranged from 2 μm to 50 μm, with a 1 μm resolution within 2–14 μm and a 2 μm resolution within 14–50 μm. To reduce the influence of ship speed on sampling, we rotated the air inlet of the instrument to be perpendicular to the ship axis. Atmospheric visibility data was collected by a CS-120 visibility meter manufactured by Campbell Scientific, Canada. This visibility meter uses a well-established forward scatter system for measuring visibility in the range from 12 to 30000 m. We set the sampling interval to 1 minute, and mounted the fog droplet spectrometer and visibility meter 3 m higher than the platform above the bridge. The distance between the two instruments was 5 m.

Fog observation was performed during navigation from outside the Arctic Ocean to the central Arctic, and can be divided into two stages: forward and back. The first stage lasted 11 days from July 23 to August 3 and the second stage lasted 22 days from August 22 to September 13 in 2016.

Fig.1 shows the navigation route. Between these two stages, some of the instruments were moved to a 21-day ice camp for joint air-ice-sea observation. Fig.2 shows a time series of fog events with visibilities less than 1000 m and durations of more than 10 minutes. We observed 26 sea fog processes during the two observation periods in the Arctic Circle, for a total of 2940 samples.

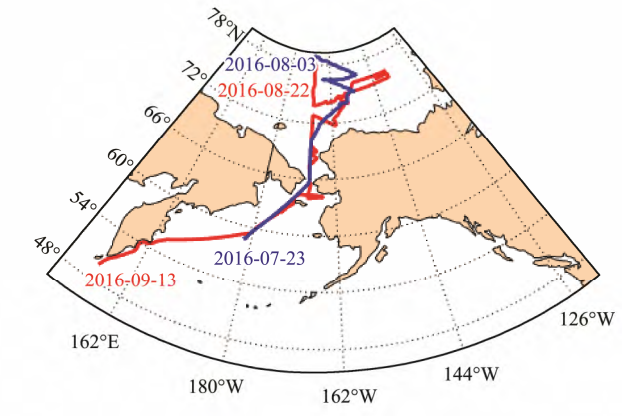

Fig.1 Navigation route for sea fog observation.

2.2 Method of Visibility Calculation

The low visibility associated with fog is caused by the scattering and absorption of light by droplets. The main component of fog droplets is water, and the absorption is weak enough to be ignored (Melchor, 1941). Therefore, the light attenuation of sea fog is mainly caused by scattering. According to the Koschmieder formula (Koschmieder, 1924), visibility V is defined as follows:

$$V = -\frac{\ln \varepsilon}{\beta}, \tag{1}$$

where ε is the brightness contrast threshold, *i.e.*, the minimum brightness contrast that can be viewed against the background by the human eye, with 0.02 typically used in meteorological observations (McCartney, 1976). The extinction coefficient β is the sum of the extinction cross-section σ_i of all fog droplets:

$$\beta = \sum_{i=1} N_i \sigma_i , \tag{2}$$

where N_i is the number of droplets of each size.

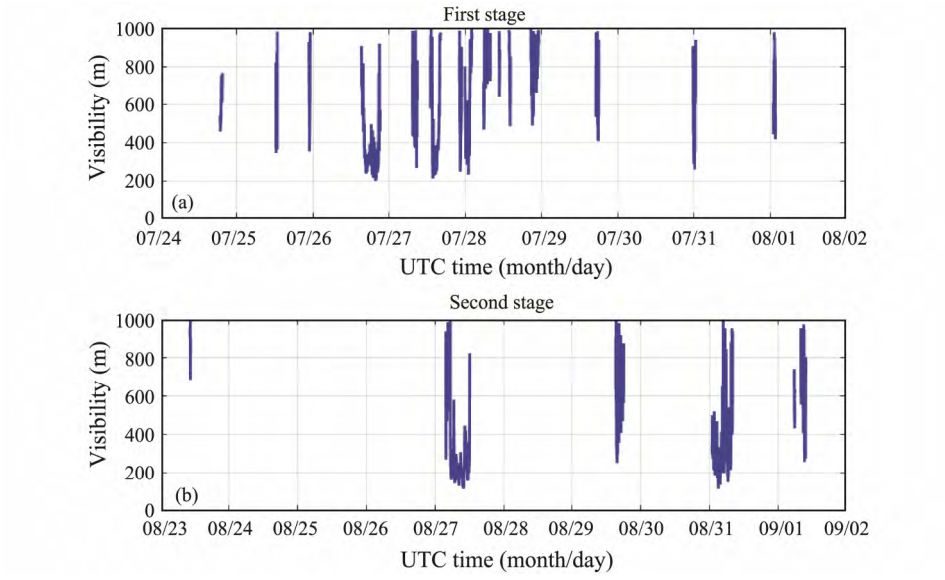

Fig.2 Time series of visibility less than 1000 m in the Arctic Circle.

According to the optical theory, Mie scattering occurs when the droplet diameter is 0.03 times greater than the wavelength of the incident light. The visible-light wavelength most sensitive to the human eye is 550 nm. The Mie theory should be used to calculate the extinction coefficient for droplet sizes ranging from 2 μm to 50 μm. The extinction effect is essentially the total light flux scattered into all directions by droplets (McCartney, 1976). According to the Mie theory (Mie, 1908), the extinction cross section of a single droplet can be calculated using Eq. (3):

$$\sigma_i = \frac{\lambda^2}{2\pi}\sum_{n=1}^{\infty}(2n+1)\left[\mathrm{Re}(a_n+b_n)\right], \tag{3}$$

where a_n and b_n are Mie coefficients:

$$\begin{cases} a_n = \dfrac{\psi_n(\alpha)\psi_n'(m\alpha) - m\psi_n'(\alpha)\psi_n(m\alpha)}{\zeta_n(\alpha)\psi_n'(m\alpha) - m\zeta_n'(\alpha)\psi_n(m\alpha)} \\ b_n = \dfrac{m\psi_n(\alpha)\psi_n'(m\alpha) - \psi_n'(\alpha)\psi_n(m\alpha)}{m\zeta_n(\alpha)\psi_n'(m\alpha) - \zeta_n'(\alpha)\psi_n(m\alpha)} \end{cases}, \tag{4}$$

where m is the complex refractive index. Because the absorption of droplets is not considered, the imaginary part of m is 0 and the real part is the refractive index of water, $m = 1.33$. The non-dimensional size parameter,

$$\alpha = 2\pi r / \lambda, \tag{5}$$

is the key parameter that determines the scattering properties. $\psi_n(x)$ and $\zeta_n(x)$ are Riccati-Bessel functions (Lentz, 1976; Wiscombe, 1980; Shen and Liu, 2005):

$$\begin{cases} \psi_0(x) = \sin(x) \\ \psi_1(x) = \dfrac{1}{x}\sin(x) - \cos(x) \\ \psi_n(x) = \dfrac{2n-1}{x}\psi_{n-1}(x) - \psi_{n-2}(x) \end{cases}, \tag{6}$$

and

$$\begin{cases} \zeta_0(x) = \sin(x) + i\cos(x) \\ \zeta_1(x) = \dfrac{1}{x}\left[\sin(x) + i\cos(x)\right] - \left[\cos(x) - i\sin(x)\right] \\ \zeta_n(x) = \dfrac{2n-1}{x}\zeta_{n-1}(x) - \zeta_{n-2}(x) \end{cases}. \tag{7}$$

$\psi_n'(x)$ and $\zeta_n'(x)$ are the derivatives of $\psi_n(x)$ and $\zeta_n(x)$:

$$\begin{cases} \psi_n'(x) = \psi_{n-1}(x) - \dfrac{n}{x}\psi_n(x) \\ \zeta_n'(x) = \zeta_{n-1}(x) - \dfrac{n}{x}\zeta_n(x) \end{cases}. \tag{8}$$

When the DSD data of sea fog is known, the extinction cross section of every single droplet can be calculated using Eq. (3), and the visibility can be calculated using Eq. (1). This method provides satisfactory calculation results for visibility when using data from a fixed position, with the relative error between the calculated result and observed visibility generally being less than 20% (Kumai, 1973). However, if the DSD data are obtained on a traveling research vessel, the calculated visibility departs significantly from the observed results. In this paper, we propose a method for calculating visibility using DSD data obtained during navigation.

3 Relation Between Calculated and Observed Visibility

The DSD and visibility data were collected during rapid navigation. In our application of the Mie theory, the calculated visibility differed significantly from the observed value. Taking the 15th sea fog process as an example (Fig.3a), when the observed visibility was less than 600 m,

the observed and calculated values are nearly the same, whereas when the observed visibility was greater than 600 m, the calculated visibility becomes much greater, even four to five times greater than the observed visibility.

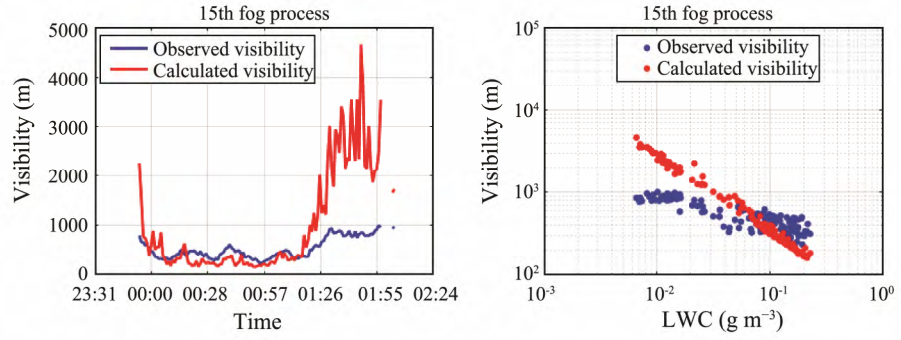

Fig.3 Comparison of calculated and observed visibilities of 15th sea fog process.

Obviously, the calculated visibility must be corrected. First, however, we must understand what happens when the deviation becomes large. To do so, we need a coordinate to express the deviation. Physically, low visibility is caused by high LWC, and there is an approximate relation, as follows (McCartney, 1976):

$$V = c(\mathrm{LWC})^{-d}. \tag{9}$$

Eq. (9) is not a strict physical law and the constants c and d vary with the spectrum of the fog droplets (Eldridge, 1971; Kumai, 1973). However, Eq. (9) suggests us to build a LWC-visibility space to embody the possible cause of the deviation between the observed and calculated visibilities. Taking the x-axis as the LWC and the y-axis as the visibility, we plotted the observed and calculated visibilities against the LWC, as shown in Fig.3b. The difference between the two visibilities is shown very clearly.

Because the LWC is determined from the DSD, the derived LWC could also deviate from the true value. The errors in the LWC and visibility do not prevent us from using the LWC-visibility space, and the reason for the errors is expected to appear in the space. Fig.4 shows the relationship among the calculated visibility, observed visibility, and LWC for all fog processes during the 2016 Arctic cruise in the LWC-visibility space, in which the abscissa is the LWC and the ordinate is visibility, with the blue points indicating the observed visibilities and the red points the calculated visibilities. Obviously, when the LWC is high, that is when the fog is heavy, the deviation between the two is small; with a reduction in the LWC, the calculated visibility is generally higher than the observed visibility. In other words, lower observed LWC causes higher calculated visibility values.

Error in the calculated visibility is expected primarily due to error in the DSD sampling during navigation (Spiegel *et al.*, 2012). Because the DSD data were sampled by active ventilation, the ship and wind speeds could push or pull the sampled air and cause turbulence pulsations at the air inlet of the fog droplet spectrometer, which can result in huge deviations in the DSD and also impact the visibility calculation. We tried to correct the calculated visibility by establishing a connection between the observed DSD and wind. The ship-based meteorological station provided the real wind speed and direction, and the ship's navigation data provided the ship's speed and heading. These two sets of data can be used to determine the relative wind speed and direction with respect to the air inlet of the fog droplet spectrometer (Fig.5).

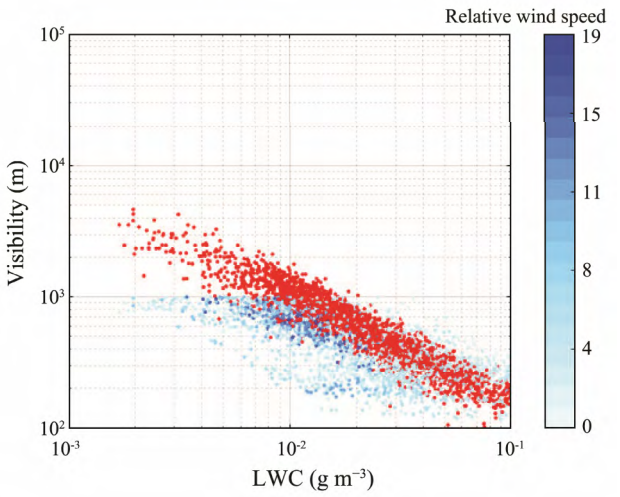

Fig.4 Relationship among calculated visibility (red points), observed visibility (red points), and LWC of all fog data.

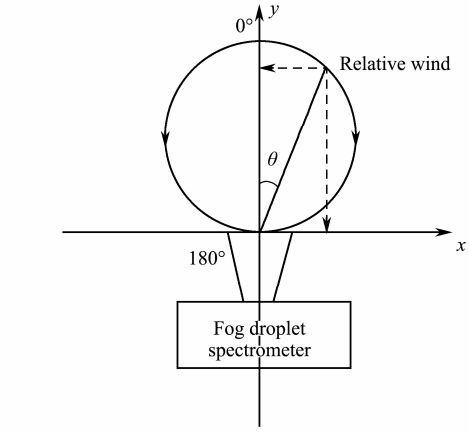

Fig.5 Relative wind speed and direction.

Let the outward direction of the inlet be the positive direction of the *y*-axis and the direction perpendicular to the inlet be the *x*-axis. Based on the analyses of the DSD data and wind direction, the DSD response at $\pm\theta$ is the same, *i.e.*, symmetrical. In the *y* direction, 0˚ indicates that the relative wind blows toward the inlet and 180˚ indicates that the relative wind blows away from the inlet. In the *x* direction, providing a symmetrical response, the *x* component of the wind is always positive.

To study the influences of the relative wind speed and direction on the calculated visibility, we must study the influences of the *x* and *y* components separately. First, in the case of the *x* component, we selected the data whose relative wind speed has a small *y* component (in the range of $[-0.5, 0.5]\,\mathrm{m\,s^{-1}}$), for a total of 362 samples. In this case, the calculated visibility is only affected by the *x* component of the wind. We categorized these data by wind speed, then linearly fitted the calculated and observed visibilities. In logarithmic coordinates, the relationship among the calculated and observed visibilities and LWC is fitted by the following:

$$\begin{cases}\log_{10} V_{ob,x} = a_{ob,x}\log_{10}\mathrm{LWC}_x + b_{ob,x}\\ \log_{10} V_{c,x} = a_{c,x}\log_{10}\mathrm{LWC}_x + b_{c,x}\end{cases}, \tag{10}$$

where subscripts *c* and *ob* are the calculated and observed values, respectively, and subscript *x* is data only affected by the wind component in the *x* direction. We fitted the data of the two stages, as shown by the solid lines in Fig.6.

Two characteristics are clearly illustrated in Fig.6. First,

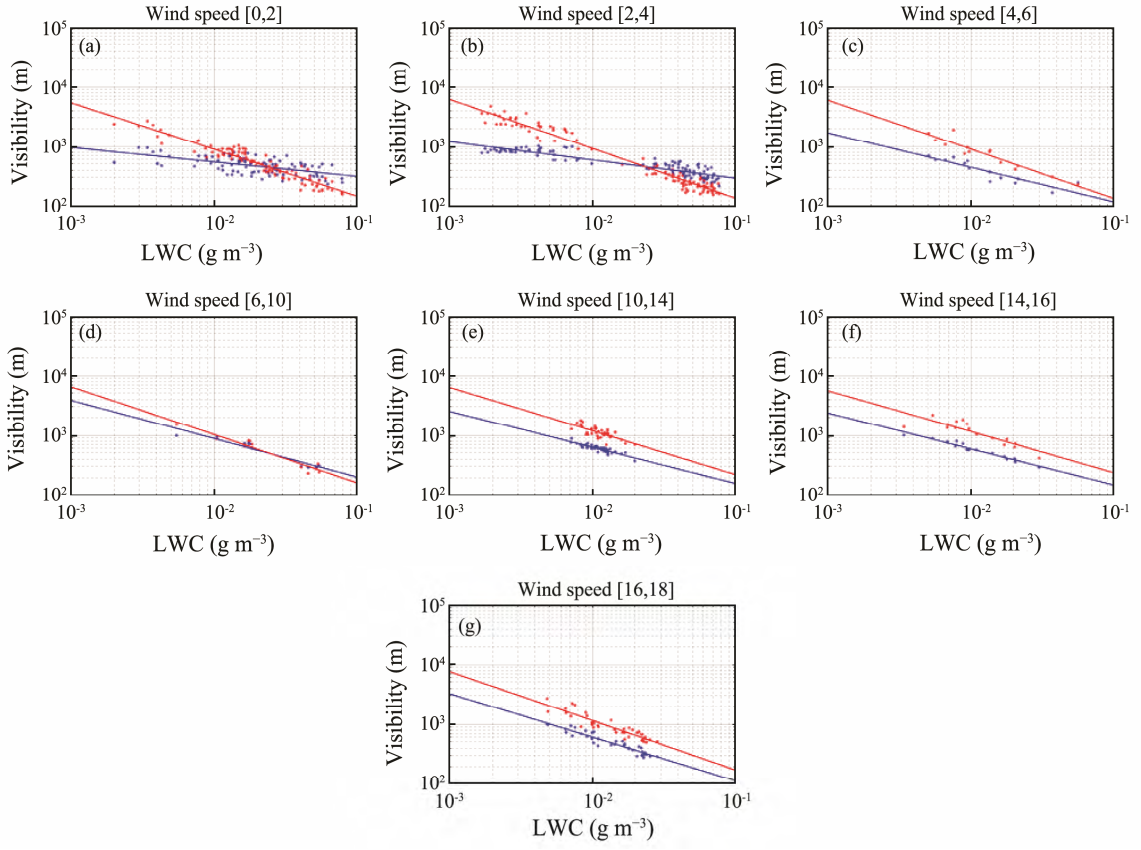

Fig.6 Fitting results of the calculated visibility (red) and observed visibility (blue) under different wind speeds in *x* direction.

regardless of the magnitude of the wind speed, the deviation of the calculated and observed visibilities increases with decreasing LWC. Secondly, the relationship of the two fitting lines within different wind speed ranges is obviously different. The angle of the two lines decreases with the increases in wind speed. When the wind speed is greater than $14\,\mathrm{m\,s^{-1}}$, the two lines are nearly parallel.

Since the calculated and observed visibilities at each moment correspond to the same LWC, the LWC in Eq. (10) can be eliminated, so:

$$\log_{10} V_{ob,x} = \frac{a_{ob,x}}{a_{c,x}}\log_{10} V_{c,x} + \left(b_{ob,x} - \frac{a_{ob,x}b_{c,x}}{a_{c,x}}\right). \tag{11}$$

Let

$$\begin{cases} a_x = \dfrac{a_{ob,x}}{a_{c,x}}\\ b_x = b_{ob,x} - \dfrac{a_{ob,x}b_{c,x}}{a_{c,x}}\end{cases}. \tag{12}$$

Then:

$$V_{ob,x} = 10^{b_x} V_{c,x}^{a_x}. \tag{13}$$

Similarly, we can select wind speed with only the *y* component when the x component of the wind speed data is in the range of $[0, 0.5]\,\mathrm{m\,s^{-1}}$, for a total of 240 samples.

Fig.7 shows the categorization and linear fitting results, in which the deviation of the calculated and observed visibilities also increases with decreasing LWC. When the wind speed is positive (the wind blows away from the inlet), the angle between the two lines increases with increased wind speed. When the wind speed is negative (the wind blows towards the inlet), this angle decreases with the increases in wind speed. Using the same method for calculating a_x and b_x, we have the following:

$$\begin{cases} a_y = \dfrac{a_{ob,y}}{a_{c,y}} \\ b_y = b_{ob,y} - \dfrac{a_{ob,y} b_{c,y}}{a_{c,y}} \end{cases}, \tag{14}$$

and

$$V_{ob,y} = 10^{b_y} V_{c,y}^{a_y}. \tag{15}$$

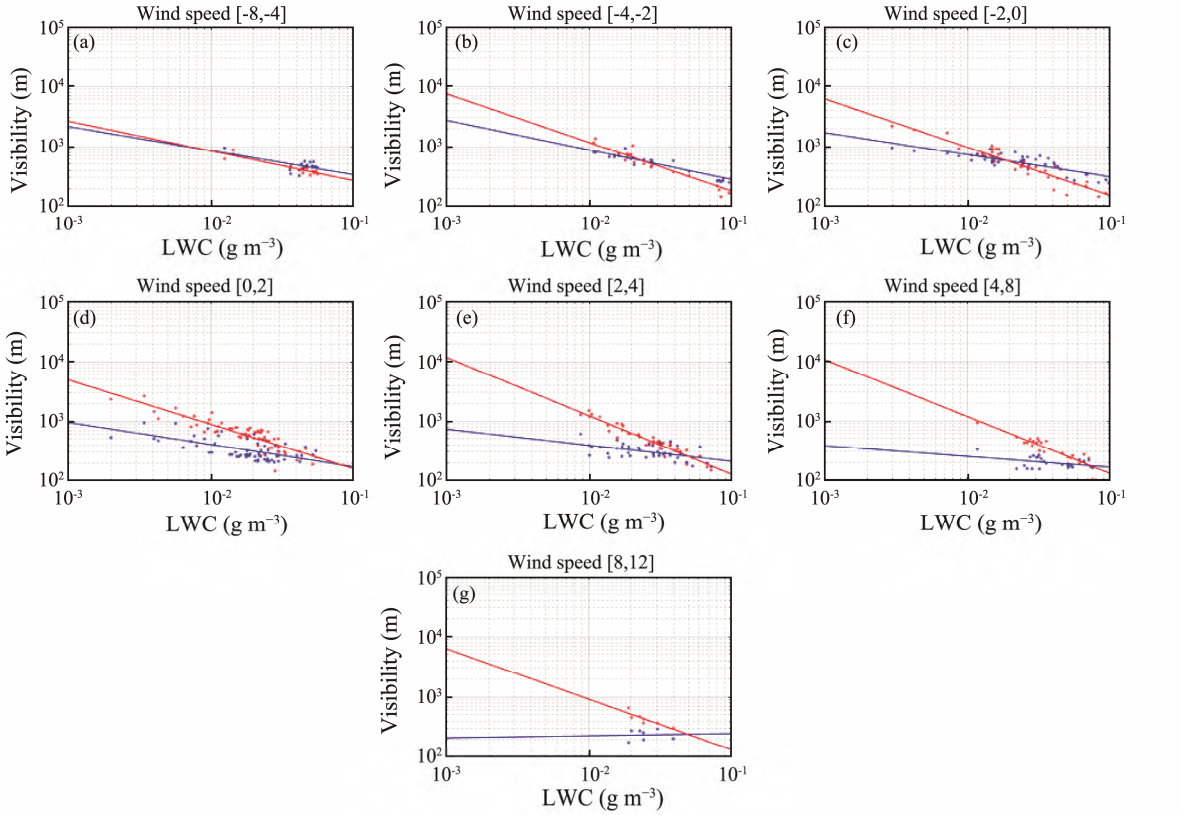

Fig.7 Fitting results of the calculated visibility (red) and observed visibility (blue) under different wind speeds in the *y* direction.

Fig.8 shows the fitting coefficients a_x, b_x, a_v, b_v derived from Eqs. (12) and (14), respectively.

With the wind speed in the *x* direction, a_x shows a monotonically increasing trend with increases in wind speed. When the wind speed is in the range of [0, 10] m s^{-1}, the increasing rate is greater than that when the wind speed is in the range of [10, 18] m s^{-1} (Fig.8a). The trend of b_x is opposite to that of a_x. With the wind speed in the *y* direction, a_y depends on the sign of the wind speed (Fig.8b). When the wind speed is positive, a_y decreases monotonically with increases in wind speed, whereas when the wind speed is negative, a_y increases monotonically with increases in wind speed. The trend of b_y is opposite to that of a_y.

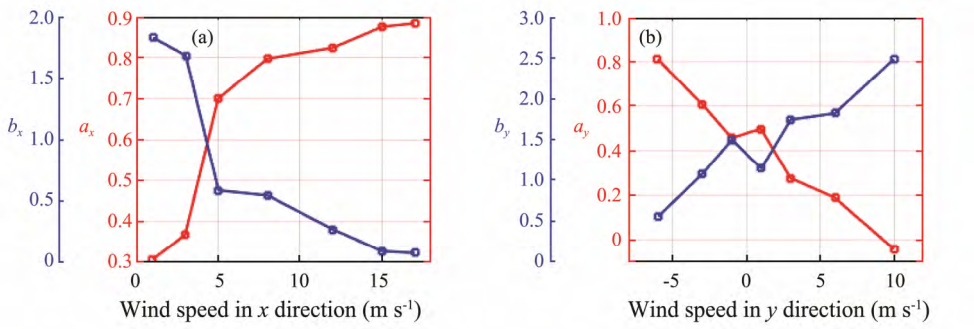

Fig.8 Fitting coefficients between observed and calculated visibilities. (a) The variation of a_x (red) and b_x (blue) with the *x* component of the wind; (b) the variation of a_v (red) and b_v (blue) with the *y* component of the wind.

The above-mentioned fitting coefficients are determined by the data obtained when the wind is in the x or y direction. These fitting coefficients can be used as correction coefficients to correct the calculated visibility under different wind situations based on Eqs. (13) and (15). Because wind can blow from any direction, the visibility can be corrected by either the x or y component, and the average and standard deviation of the absolute errors of the calculated visibility are shown in Fig.9. Absolute errors are classified in terms of LWC in the range of [0.001, 0.1] $\mathrm{g\,m^{-3}}$ with a resolution of $0.01\,\mathrm{g\,m^{-3}}$. It is clear that the calculated visibility is greatly improved even when using only the x or y components of wind speed, especially when the LWC is low. The standard deviation corrected by Eq. (13) is slightly better than that by Eq. (15).

In general, better correction results can be obtained by either Eq. (13) or Eq. (15), which shows the absolute necessity of correction. However, there is a slight difference between the two correction results. We hope to establish a more general correction method than Eq. (13) or Eq. (15). To take both wind components into consideration, we introduce θ, which is shown in Fig.5. The correction coefficients related to the relative wind direction can be derived from a_x, b_x, a_y, b_y and θ, as follows:

$$\begin{cases} a = (1-\sin\theta)\cdot a_y + \sin\theta\cdot a_x \\ b = (1-\sin\theta)\cdot b_y + \sin\theta\cdot b_x \end{cases}, \tag{16}$$

and the calculated visibility can be corrected by the following equation:

$$V_{ob} = 10^b V_c^a . \tag{17}$$

The average and standard deviation of the absolute error of the visibility, corrected using Eq. (17), are shown in Fig.9 by the green dotted lines. When the wind direction θ is taken into account, the average and standard deviation are basically consistent with the minimum value of those calculated following Eqs. (13) and (15). The correction results are improved by eliminating the fluctuations in the correction of individual wind components.

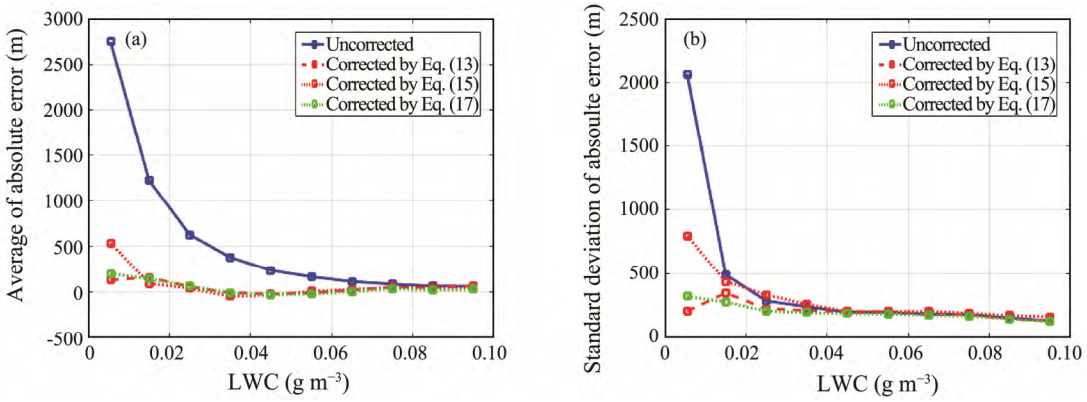

Fig.9 Comparison of different correction methods. Average of absolute error (a) and the standard deviation of absolute error (b). The blue solid lines are the uncorrected calculated visibilities, red dashed lines are the calculated visibilities corrected by Eq. (13), red dotted lines are the calculated visibilities corrected by Eq. (15), and the green dotted lines are the calculated visibilities corrected by Eq. (17).

Next, we corrected the calculated visibilities for all the fog data by the weighted correction method that considers the relative wind direction. Fig.10 shows a comparison of the observed visibility, corrected visibility, and the visibility calculated by the Mie theory only. We can see that the error of the calculated visibility after correction is much better than before.

4 Conclusions

Sea fog data is typically obtained using two kinds of measuring instruments, a fog droplet spectrometer for DSD and a visibility meter for atmospheric visibility. The LWC can be derived from the DSD data. The visibility reduction caused by fog is due to the scattering of light by fog droplets. The relationship of the DSD and visibility reflects the physical connection between the scattering of large particles and visibility, which is important for understanding the formation mechanism and impact of sea fog. Therefore, visibility can be calculated from DSD data. For measurements on land, the relationship between DSD and visibility established by the Mie theory has been relatively reliable with an error of less than 20%. During land-based observation, we can point the air inlet of the fog droplet spectrometer into the local prevailing wind, which minimizes the influence of wind from other directions on the DSD data sampling. But for data observation on a traveling vessel, the constantly changing ship speed and heading means that wind blows from every direction into the inlet of the fog droplet spectrometer, so the visibility calculated by the Mie theory using DSD data has serious errors compared to the observed results. This error is obviously caused by the strong relative wind inherent in navigation. In this paper, we calculated the visibility by the Mie theory from sea fog DSD data obtained during the 2016 Chinese Arctic Scientific Expedition and then compared it with the observed visibility. The analysis of error for the wind perpendicular (x direction) and parallel (y direction) to the inlet shows that the direction compo nents have different effects on the visibility calculation.

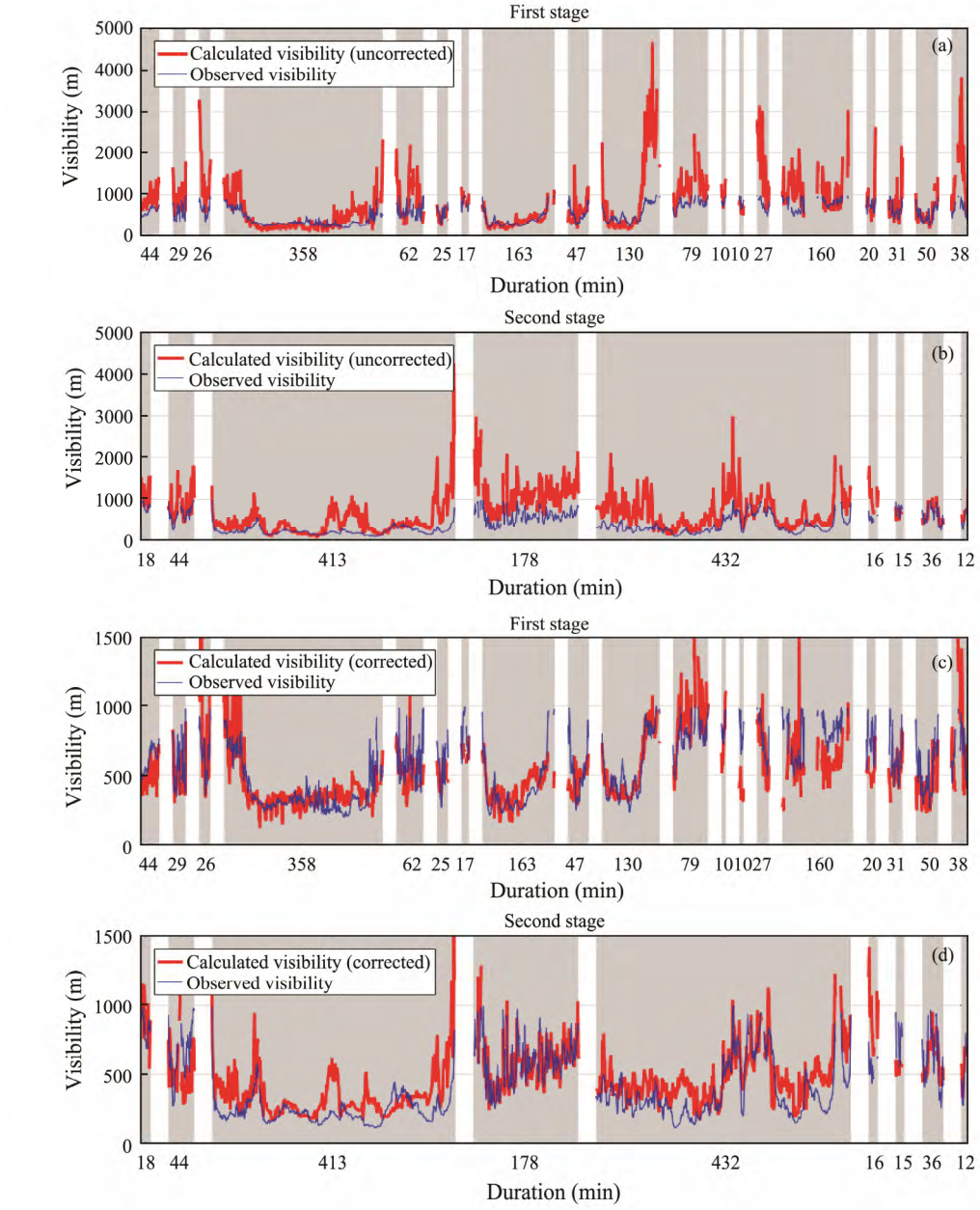

Fig.10 Comparison of observed visibility with uncorrected and corrected calculated visibilities from the two sea fog observation stages. Blue lines indicate the observed visibility, and red lines the uncorrected calculated visibility (a, b) and corrected calculated visibility (c, d). Gray background color indicates a sea fog process, as distinguished from white. The abscissa is the duration of each sea fog process.

We provide two sets of correction coefficients for the *x* and *y* wind components, respectively, based on which we propose a correction method that takes into account the relative wind speed and direction.

In our study, the calculated visibility was greatly improved by the proposed correction method. We found that when the LWC is low, the influence of the wind becomes very important, and the uncorrected calculated visibility obviously deviates from the observed visibility. The corrected results show that the calculated visibility can be effectively corrected to obtain satisfactory results. When the LWC is high, the uncorrected calculated visibility and observed visibility are very similar, and the calculated visibility does not change much after correction. The effect of this correction method is increased with decreases in the LWC. The standard algorithm and correction method proposed in this paper can be applied in visibility calculations from DSD data measured during navigation.

During navigation, apart from major factors such as wind and sailing, other factors may also affect the visibility calculation. The temperature of the ship body may change the DSD structure and an inappropriate distance between the fog droplet spectrometer and visibility meter may mean that the two instruments are unable to simultaneously observe the same fog area. Therefore, these two instruments should be installed as far as possible from the ship hull and not too far from each other. In addition, the FM-120 fog droplet spectrometer cannot observe droplets

whose diameters range from 0–2 μm, so the influence of these droplets on visibility calculations made during navigation requires further observation and research.

Acknowledgements

This work was supported by the National Natural Science Foundation of China (No. 41330960), the National Major Science Project of China for Global Change Research (No. 2015CB953900), and the Major State Basic Research Development Program (No. 2016YFC1402702).

References

Eldridge, R. G., 1971. The relationship between visibility and liquid water content in fog. *Journal of Atmospheric Sciences*, **28** (7): 1183-1186.

Garland, J., 1971. Some fog droplet size distributions obtained by an impaction method. *Quarterly Journal of the Royal Meteorological Society*, **97** (414): 483-494.

Gultepe, I., Kuhn, T., Pavolonis, M., Calvert, C., Gurka, J., Heymsfield, A. J., Liu, P. S. K., Zhou, B., Ware, R., Ferrier, B., Milbrandt, J., and Bernstein, B., 2014. Ice fog in Arctic during FRAM–Ice Fog Project: Aviation and nowcasting applications. *Bulletin of the American Meteorological Society*, **95** (2): 211-226.

Gultepe, I., Tardif, R., Michaelides, S. C., Cermak, J., Bott, A., Bendix, J., Müller, M. D., Pagowski, M., Hansen, B., Ellrod, G., Jacobs, W., Toth, G., and Cober, S. G., 2007. Fog research: A review of past achievements and future perspectives. *Pure and Applied Geophysics*, **164** (6-7): 1121-1159.

Houghton, H. G., and Radford, W. H., 1938. On the measurement of drop size and liquid water content in fogs and clouds. *Papers in Physical Oceanography and Meteorology*, **6** (4): 10-29.

Koračin, D., Dorman, C. E., Lewis, J. M., Hudson, J. G., Wilcox, E. M., and Torregrosa, A., 2014. Marine fog: A review. *Atmospheric Research*, **143**: 142-175.

Koschmieder, H., 1924. Theorie der horizontalen Sichtweite. *Beitrage zur Physik der freien Atmosphare*, **12**: 33-53.

Kumai, M., 1973. Arctic fog droplet size distribution and its effect on light attenuation. *Journal of the Atmospheric Science*, **30** (4): 635-643.

Lentz, W. J., 1976. Generating Bessel functions in Mie scattering calculations using continued fractions. *Applied Optics*, **15** (3): 668-671.

McCartney, E. J., 1976. *Optics of the Atmosphere: Scattering by Molecules and Particles, Book Review*. John Wiley and Sons, Inc., New York, 1-421.

Melchor, C. V., 1941. The Refractive index of liquid water in the near infra-red spectrum. *Journal of the Optical Society of America*, **31** (3): 244.

Mie, G., 1908. Beiträge zur Optik trüber Medien, speziell kolloidaler Metallösungen. *Annalen der Physik*, **330** (3): 377-445.

Ogiwara, S., and Okita, T., 1952. Electron microscope study of cloud and fog nuclei. *Tellus*, **4** (3): 233-240.

Palm, S. P., Strey, S. T., Spinhirne, J., and Markus, T., 2010. Influence of Arctic sea ice extent on polar cloud fraction and vertical structure and implications for regional climate. *Journal of Geophysical Research: Atmospheres*, **115**: D21209.

Roach, W. T., 1976. On the effect of radiative exchange on the growth by condensation of a cloud or fog droplet. *Quarterly Journal of the Royal Meteorological Society*, **102** (432): 361-372.

Shen, J. Q., and Liu, L., 2005. An improved algorithm of classical Mie scattering calculation. *China Powder Science and Technology*, **11** (s1): 45-50 (in Chinese with English abstract).

Shupe, M. D., and Intrieri, J. M., 2004. Cloud radiative forcing of the Arctic surface: The influence of cloud properties, surface albedo, and solar zenith angle. *Journal of Climate*, **17** (3): 616-628.

Spiegel, J. K., Zieger, P., Bukowiecki, N., Hammer, E., Weingartner, E., and Eugster, W., 2012. Evaluating the capabilities and uncertainties of droplet measurements for the fog droplet spectrometer (FM-100). *Atmospheric Measurement Techniques*, **5** (9): 2237-2260.

Venne, M. G., Jasperson, W. H., and Venne, D. E., 1997. Difficult Weather: A Review of thunderstorm, fog and stratus, and winter precipitation forecasting. Augsburg Coll Minneapolis MN Center for Atmospheric and Space Sciences, Minneapolis, 1-54.

Wang, B. H., 1983. *Sea Fog*. China Ocean Press, Beijing, 1-102 (in Chinese).

Wiscombe, W. J., 1980. Improved Mie scattering algorithms. *Applied Optics*, **19** (9): 1505-1509.

(Edited by Chen Wenwen)